Role of intermediate phase for stable cycling of $Na_7V_4(P_2O_7)_4PO_4$ in sodium ion battery

Soo Yeon Lim[a,1], Heejin Kim[a,1], Jaehoon Chung[b], Ji Hoon Lee[a], Byung Gon Kim[a], Jeon-Jin Choi[c], Kyung Yoon Chung[c], Woosuk Cho[d], Seung-Joo Kim[b], William A. Goddard III[a,e,2], Yousung Jung[a,f,2], and Jang Wook Choi[a,f,2]

[a]Graduate School of Energy, Environment, Water, and Sustainability, World Class University, Korea Advanced Institute of Science and Technology, Yuseong-gu, Daejeon 305-701, Korea; [b]Department of Chemistry, Division of Energy Systems Research, Ajou University, Yeongtong-gu, Suwon 443-749, Korea; [c]Center for Energy Convergence, Korea Institute of Science and Technology, Seongbuk-gu, Seoul 136-791, Korea; [d]Advanced Batteries Research Center, Korea Electronics Technology Institute, Bundang-gu, Seongnam-si, Gyeonggi-do 463-816, Korea; [e]Materials and Process Simulation Center, California Institute of Technology, Pasadena, CA 91125; and [f]Institute NanoCentury, Korea Advanced Institute of Science and Technology, Yuseong-gu, Daejeon 305-701, Korea

Contributed by William A. Goddard III, September 9, 2013 (sent for review July 21, 2013)

Sodium ion batteries offer promising opportunities in emerging utility grid applications because of the low cost of raw materials, yet low energy density and limited cycle life remain critical drawbacks in their electrochemical operations. Herein, we report a vanadium-based ortho-diphosphate, $Na_7V_4(P_2O_7)_4PO_4$, or VODP, that significantly reduces all these drawbacks. Indeed, VODP exhibits single-valued voltage plateaus at 3.88 V vs. Na/Na^+ while retaining substantial capacity (>78%) over 1,000 cycles. Electronic structure calculations reveal that the remarkable single plateau and cycle life originate from an intermediate phase (a very shallow voltage step) that is similar both in the energy level and lattice parameters to those of fully intercalated and deintercalated states. We propose a theoretical scheme in which the reaction barrier that arises from lattice mismatches can be evaluated by using a simple energetic consideration, suggesting that the presence of intermediate phases is beneficial for cell kinetics by buffering the differences in lattice parameters between initial and final phases. We expect these insights into the role of intermediate phases found for VODP hold in general and thus provide a helpful guideline in the further understanding and design of battery materials.

cathode | single voltage | atomic reorganization | ab initio calculation

Sodium ion batteries (SIBs) provide advantages of unlimited resource, low material cost, and easy worldwide accessibility that could make them the material of choice for grid-scale energy storage systems (1, 2). Unfortunately, the electrochemical performance of current SIBs remains inferior to that of lithium ion batteries (LIBs). In particular, we require SIB cathode materials that give a long cycle life with large capacities and high voltages under fast operating conditions, comparable to the Li counterparts.

Numerous layered Na_xMO_2 [M = Co, Mn, Fe, Ni, Cr, and multicomponent transition metals (TMs)] have been intensively studied as candidate SIB cathodes because such layer-structured materials typically exhibit higher capacities than other classes of materials (3–10). However, they suffer from a substantial capacity decay with cycling, owing to crystal structure collapse and/or unstable electrode–electrolyte interfaces (10). For more stable host frameworks, various polyanion structures have also been studied as SIB cathodes as a natural extension of the success shown in the LIB materials of the same classes, including TM fluorophosphates (11–15), pyrophosphates (16–18) and phosphates (19–22). However, most of these materials still exhibited insufficient cycle lifetimes and large voltage steps that limit their practical capacity. The Prussian blue family has also been extensively investigated for both organic (23, 24) and aqueous electrolytes (25) owing to its unique advantages related to low material cost, low temperature synthesis, and decent electrochemical performance from well-developed ionic channel structures. However, the as-synthesized Prussian blue family is usually in the potassium form and thus requires ion exchange with Na ions.

Herein, we report a vanadium-based ortho-diphosphate, $Na_7V_4(P_2O_7)_4PO_4$, or VODP, that addresses these limitations of the present SIB cathodes. By engaging the V^{3+}/V^{4+} redox couple, VODP exhibits single well-defined voltage plateaus at 3.88 V vs. Na/Na^+, which is optimal for stable operations within a usable electrolyte window. Combined with the robust host frameworks, VODP exhibits unprecedented cycle life, maintaining substantial capacity retention over 1,000 cycles. In particular, we find that the observed single plateau and long cycle life is due to the existence of a very shallow intermediate phase along the battery reaction, a concept that can be used to understand existing electrochemical properties or for future developments. To this end, we also propose a simple theoretical method to estimate the reaction barrier for two-phase reactions in general.

Results and Discussion

Synthesis and Crystal Structure of $Na_7V_4(P_2O_7)_4PO_4$. $Na_7V_4(P_2O_7)_4PO_4$, or VODP, was synthesized by simple solid state reactions. For this, stoichiometric amounts of precursors, sodium carbonate (Na_2CO_3), vanadium pentoxide (V_2O_5), and ammonium phosphate ($NH_4H_2PO_4$), were first mixed thoroughly and then reacted at 800 °C under argon atmosphere. Detailed synthetic procedures

Significance

Utilizing low-cost materials, sodium ion batteries (SIBs) are beginning to attract considerable attention, particularly for large-scale utility grid applications. However, electrochemical performance of most SIB active materials is still insufficient for various practical applications. In the current study, we discovered a vanadium-based ortho-diphosphate, $Na_7V_4(P_2O_7)_4PO_4$, or VODP, that holds exceptional electrochemical properties represented by well-defined high voltage profiles at 3.88 V (vs. Na/Na^+) and substantial capacity retention over 1,000 cycles. A theoretical analysis suggests that an intermediate phase encountered during phase transformation of VODP is crucial for better kinetics during battery operations, which can be expanded as a general principle in understanding diverse battery materials.

Author contributions: S.Y.L., H.K., W.A.G., Y.J., and J.W.C. designed research; S.Y.L., H.K., J.C., J.H.L., B.G.K., J.-J.C., K.Y.C., W.C., S.-J.K., and J.W.C. performed research; S.Y.L., H.K., J.C., J.H.L., B.G.K., K.Y.C., W.C., S.-J.K., W.A.G., Y.J., and J.W.C. analyzed data; and S.Y.L., H.K., J.-J.C., W.A.G., Y.J., and J.W.C. wrote the paper.

The authors declare no conflict of interest.

Data deposition: Further details of the crystal structure of $Na_7V_4(P_2O_7)_4PO_4$ may be obtained from Fachinformationszentrum Karlsruhe, 76344 Eggenstein-Leopoldshafen, Germany [Cambridge Structural Database (CSD) nos. CSD-427133 (neutron) and CSD-427134 (X-ray)].

[1]S.Y.L. and H.K. contributed equally to this work.

[2]To whom correspondence may be addressed. E-mail: wag@wag.caltech.edu, ysjn@kaist.ac.kr, or jangwookchoi@kaist.ac.kr.

This article contains supporting information online at www.pnas.org/lookup/suppl/doi:10.1073/pnas.1316557110/-/DCSupplemental.

are described in *Materials and Methods*. The crystal structure was resolved by analyzing the complementary X-ray diffraction (XRD) and neutron diffraction (ND) patterns (Fig. 1 *A* and *B*) together. VODP exhibits the tetragonal P-42_1c space group with lattice parameters a = 14.225(3) Å and c = 6.364 (17) Å (Tables S1 and S2). Although the diffraction patterns include peaks from a small amount (<4%) of $Na_3V_2(PO_4)$ as an impurity (26, 27), these impurity peaks are well separated from those of the VODP phase, at least in the low and medium angle regions. An SEM image shown in Fig. 1*B*, *Inset* indicates that the solid state reaction produced particles with dimensions in the range of 1–3 μm.

As shown in Fig. 1*C*, the structure of VODP can be described by the repetition of a basic unit, $(VP_2O_7)_4PO_4$, using fourfold symmetry (dotted line in Fig. 1*C*). In the $(VP_2O_7)_4PO_4$ unit, a central tetrahedron [PO_4] shares corners with four [VO_6] octahedra, and each diphosphate group [P_2O_7] bridges the two adjacent [VO_6] octahedra by sharing the corners. The interconnected $(VP_2O_7)_4PO_4$ units form a 3D framework with well-defined ionic channels for Na (de)insertion. Na ions (Fig. 1*D*) occupy three different crystallographic positions, Na1, Na2, and Na3, adopting bipyramidal, square planar, and tetrahedral coordinations, respectively. A transmission electron microscopy image and its fast Fourier transformation pattern confirm the particle dimensions and the given crystal structure (Fig. S1). Although the isostructures, $Na_7M_4(P_2O_7)_4PO_4$ (M = Al, Cr, and Fe), have been investigated (28), the vanadium version of this framework has been neither reported as a battery electrode material nor even documented in the materials database.

Electrochemical Properties of $Na_7V_4(P_2O_7)_4PO_4$. To evaluate VODP as an SIB cathode, coin-type half cells were prepared in which sodium thin disks were used as both the reference and counter electrodes. The galvanostatic profiles measured at C/40 and C/20 rates (Fig. 2*A*) exhibit single well-defined plateaus at 3.88 V throughout both charging and discharging processes. The potential of 3.88 V is quite noticeable considering that this material does not contain fluorine to increase the inductive effect (29), and the cell voltages of SIBs are generally lower than those of LIBs by 0.2–0.6 V (30).

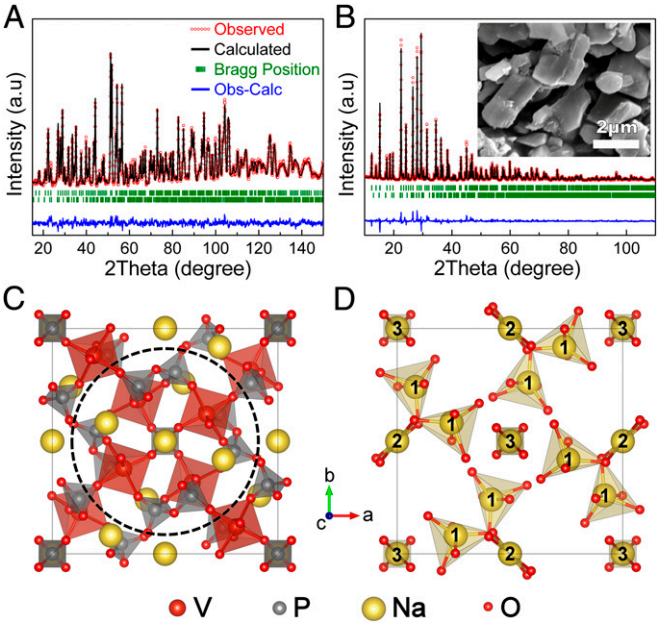

Fig. 1. (*A*) Neutron and (*B*) X-ray diffraction patterns of $Na_7V_4(P_2O_7)_4PO_4$ and their Rietveld refinement profiles: observed (red open circles), calculated (black line), and difference (blue line). Bragg positions for both $Na_7V_4(P_2O_7)_4PO_4$ (upper green) and $Na_3V_2(PO_4)_3$ (minor phase, lower green) are also presented. The inset in *B* shows an SEM image of as-synthesized sample. (*C*) A projected crystal structure along the c axis. Gray tetrahedrons, PO_4; red octahedrons, VO_6; yellow spheres, Na atoms. The $(VP_2O_7)_4PO_4$ unit is denoted as a dashed circle. (*D*) Schematic illustration of the various Na sites (Na1~Na3) projected along the same c-axis.

The galvanostatic data (Fig. 2*A*) measured at C/40 indicate that capacities are 81.5 and 77.1 mAh·g^{-1} for charge and discharge, respectively, which correspond to 3.5 and 3.3 Na ions per each formula unit of $Na_7V_4(P_2O_7)_4PO_4$. At C/20, the charge and discharge capacities are 78.5 and 73.6 mAh·g^{-1}, respectively. These values imply that four Na ions per each formula unit are theoretically available (92.8 mAh·g^{-1}) in this material within the given potential window (2.0–4.2 V vs. Na/Na$^+$).

The differential capacity (dQ/dV) data (Fig. 2*B*) exhibit a discrepancy between charging and discharging peaks. When measured at C/20, the charging profile shows two separate peaks at 3.88 and 3.92 V, whereas the discharging profile shows only a single peak at 3.86 V. Such distinctive behavior between the charge and discharge is similar to the case of $NaFePO_4$ (19, 20), where the origin is speculated to be the different reaction pathways during charge and discharge (19). However, in VODP the distinctive behavior is likely to be attributed to different kinetics, rather than different reaction pathways, from the quasi-open circuit potential (QOCP) result (Fig. 2*C*). Whereas the QOCP profile confirms the equilibrium potentials at 3.87 V and 3.89 V, the profile indicates two separate regions, the first half with small polarizations (7 mV) and the other half with relatively larger polarizations (30 mV and 20 mV for charge and discharge, respectively). From this, it is anticipated that the split peaks during the charge in the dQ/dV data are related to these two separate regions with their distinctive kinetics. However, the two peaks in the dQ/dV data become merged during the discharge scanned in the reverse direction owing to the larger polarizations of the second half region. The split peaks in the dQ/dV data also indicate the existence of one stable intermediate phase around $x = 5$ in $Na_xV_4(P_2O_7)_4PO_4$. It is anticipated that the large polarizations observed at the end of charge and discharge originate from the smaller electronic conductivities of the fully charged and discharged phases where all vanadium atoms are oxidized to V^{4+} and reduced to V^{3+}, respectively. As evidence of this scenario, we find that the large polarizations disappeared upon integration with reduced graphene oxide (rGO), which decreases electrical impedance on the electrode film scale by reducing electronic transport length (Fig. S2*A*).

The bare VODP without carbon coating exhibits stable cycling (Fig. 3*A*), such as 92.6% retention after 50 cycles, using the intrinsic characteristics of this material such as the corner sharing of polyhedrons that accommodates structural changes and the spectator portions (Na_3 and PO_4) that do not participate in the electrochemical reaction but contribute to stability of the framework. Furthermore, we integrated VODP with rGO (Fig. S2) because rGO integration has been known to diminish the resistances between particles and improve electrochemical performance (31–34). Upon rGO integration, VODP retains 89.7% and 78.3% of the initial capacity (91.0 mAh·g^{-1}) even after 500 and 1,000 cycles (Fig. 3*B*), respectively. The small volume change (2.4%) for VODP may play a role in this robust electrochemical operation. The rate and cycling performances of the rGO-integrated and bare samples measured under different conditions are presented in Fig. S3. It should be noted that the bare VODP without rGO integration shows reasonably good performance even in the micrometer dimension (Fig. S3*E*): 78.9% capacity retention after 100 cycles when measured at C/2 and 75.9% capacity retention (78.4 → 59.5 mAh·g^{-1}) upon the C-rate increase from C/40 to C/2.

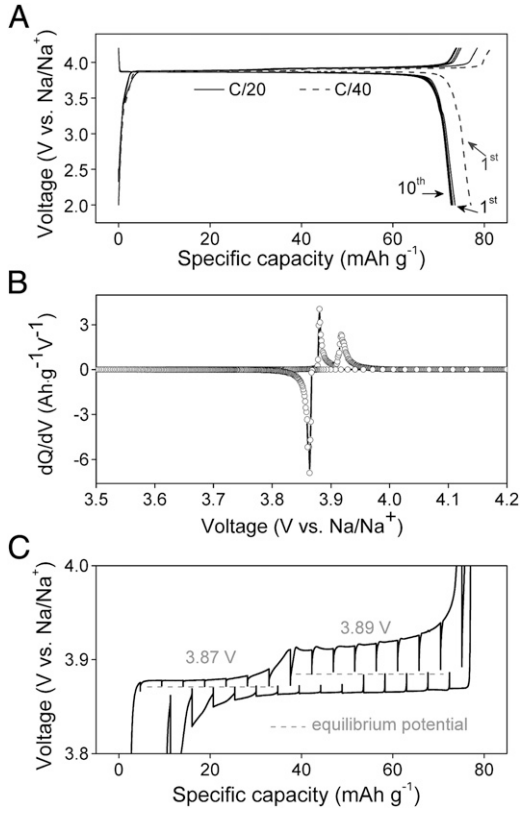

Fig. 2. (*A*) Galvanostatic profiles of $Na_7V_4(P_2O_7)_4PO_4$ measured at C/20 and C/40 in the first cycles. The profiles at C/20 in the cycle range of 2∼10 are also presented. (*B*) The differential capacity curve (dQ/dV) obtained from the galvanostatic profile. (*C*) A QOCP profile measured at C/20.

Intermediate Phase and Single-Valued Plateaus. To obtain deeper insights into the charging/discharging processes, we performed ex situ XRD measurements (Fig. 4*A*) and density functional theory (DFT) calculations.

In the first charge, consistent with the QOCP data, the ex situ XRD analyses show distinctive spectra for the first and second halves of the curve. On the first plateau (2 in Fig. 4*A*), namely, the two-phase region between the pristine and intermediate phases, the split peaks were observed at the 2θ range of 22–30°, indicating that the intermediate phase is structurally very close to the pristine phase. During the second half of the charge (3→5), the two-phase region between the intermediate and fully charged phases, new peaks gradually grow in corresponding to the fully charged phase, eventually reaching a new spectrum at the end of the charging (5). The smaller polarization in the first half compared with the second half (7 mV vs. 20–30 mV) may be associated with the smaller volume change (0.4% vs. 2.0% from Fig. S4). This point will be discussed below. The spectra during the discharge in the same cycle show largely reversed peak changes, indicative of reversible phase transformation of $Na_7V_4(P_2O_7)_4PO_4$ during Na insertion and deinsertion. The same peak changes were consistently observed for the second charge as well.

The calculated and experimental diffraction spectra for both pristine and fully charged phases are in excellent agreement as shown in Fig. 4*A* (blue and red lines). Fig. 4*B* illustrates the phase transformation of the crystal structure during charging. We denote the structurally similar pristine and intermediate phases as A-type and the fully-charged phase as B-type. When the structure transforms from the A-type to the B-type phases, each unit of $(VP_2O_7)_4PO_4$ (dashed squares in Fig. 4*B*) rotates clockwise and counterclockwise symmetrically by 11.7°. As a result, in the B type, the repeated units of $(VP_2O_7)_4PO_4$ are aligned in a more orderly fashion with the neighboring units. One can compare the green shaded regions of both structures in Fig. 4*B*. The activation barrier for the rotation of the $(VP_2O_7)_4PO_4$ unit is calculated to be ∼60 meV (Fig. S5), implying that the latter structural change is energetically almost free and hence does not compromise the reversibility of this material upon cycles. This nearly barrierless rotation can be understood as follows. Because all of the four active Na ions are extracted from the Na1 sites (orange spheres in Fig. 4*B*), the original structural distortion that was needed to stabilize the Na1 ions in the bipyramidal units is now released in the charged state. During this relaxation, the overall crystal structure rearranges to stabilize the remaining Na2 sites (violet spheres in Fig. 4*B*) via the transformation from the square planar to the tetrahedral units (green arrows in Fig. 4*B*). Therefore, the relative stability of Na1 and Na2 sites and their occupation govern the phase transformation between A- and B-type phases as shown in Fig. 4*C* (red being more stable after $x = 5$).

The calculated convex hull connecting the minimum formation energies at different x values (Fig. 4*C*) confirms the experiments that the A-type intermediate phase indeed exists at $x = 5$, albeit extremely shallow, yielding almost single-valued plateaus. The formation of such an intermediate phase is attributed to the exceptional Na and V^{3+}/V^{4+} orderings at $x = 5$ (Fig. S6), where relatively stronger electrostatic repulsions between Na^+ and V^{4+} ions allow the close proximity of Na^+ and V^{3+} ions.

The present material shows a desirable single-valued voltage plateau as shown in Fig. 2. Although all of the Na ions involved in the reaction are from the equivalent crystallographic sites (Na1) throughout the entire charging process, the single-valued plateaus are indeed peculiar because the current material experiences the phase transformations that would not any more leave all of the Na sites in the same environments. That is, structurally, the host material undergoes significant geometric rotations during the second half of the charge as discussed above, but energetically the material maintains the energy loss (gain) for the Na extraction (insertion) almost constant

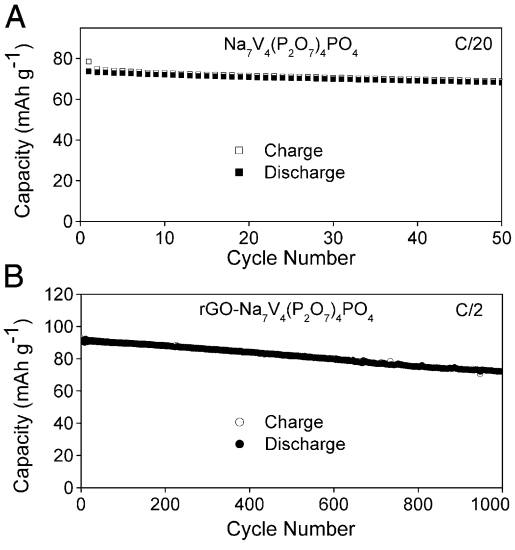

Fig. 3. The capacity retentions of (*A*) bare and (*B*) rGO integrated samples. In both *A* and *B*, the rates for charge and discharge are the same in each cycle. In *B*, the specific capacities were calculated based on the mass of $Na_7V_4(P_2O_7)_4PO_4$ only because the exclusive contribution from rGO is difficult to be isolated. From a control experiment based on rGO only, we found that rGO has its own capacity of ∼38 mAh·g^{-1} in the given potential range.

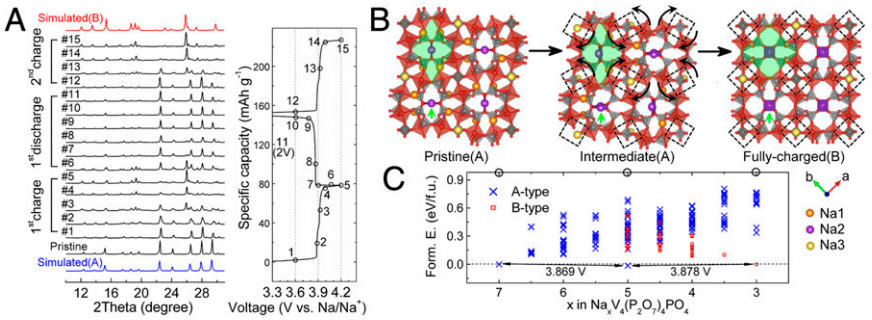

Fig. 4. (*A*) Ex situ XRD spectra obtained at the points denoted in the galvanostatic curve on the right-hand side. The XRD spectra of the A-type and B-type phases simulated from the DFT calculations are also presented (blue and red lines). (*B*) The structure rearrangement during phase transformation between pristine and charged phases. Crystallographically different sodium sites are colored with different colors (Na1, orange; Na2, violet; Na3, yellow). (*C*) Formation energies of the A- and B-type phases and the estimated voltages obtained from calculations.

throughout the entire charge (discharge). In other words, the amount of stabilization for the charge ordering in the intermediate phase is similar to that for the framework rotation in the fully charged phase.

Presence of Intermediate Phases for Better Kinetics. The "interfacial energy penalty" between adjacent phases is an important factor in two-phase reactions, especially when kinetics is limited by the secondary phase nucleation and growth that should be overcome for charging and discharging. It typically arises from atomic reorganizations such as rotation, elongation, breaking, and forming of bonds. Therefore, to incorporate the latter effects into the theoretical framework, the following issues need to be addressed: (*i*) the reorganization depends on a large number of degrees of freedom; (*ii*) although the initial and final states (or reactant and product) of the reaction are clearly known, the transition state (TS) that determines the kinetics is not, and thus consequently (*iii*) the reorganization energy associated with phase boundary migration is difficult to quantify.

To resolve the second and third problems, we can draw relative energy penalties compared with the equilibrium (bulk) state as a function of a "proper" predefined reaction coordinate (Fig. 5*A*). Here, the reactant and product are phases A and B, respectively, and the reaction is the phase transformation from A to B. We define the coordinate R_m that minimizes a sum of energy penalties to be the TS, and the total energy penalty at R_m, $E(R_m) = E_A(R_m) + E_B(R_m)$, to be the activation energy of the reaction. We note that the solution R_m satisfies two conditions at TS: the same "lattice coordinates" and "forces" (slopes) with opposite sign for the two phases. For example, for a one-dimensional lattice model, the former and latter conditions would ensure the lattice match and force equilibrium, respectively, at TS.

The first problem, a large number of degrees of freedom, can be addressed by choosing a collective variable that can represent the reaction progress properly. One good example of a collective variable for reorganizations in solids might be the lattice parameters that have also been often used to explain kinetics of cathode materials in the battery field (35). Because the cathode materials have a coherent or semicoherent interface between charged and discharged phases (36), the lattice parameters evolve gradually between those of the two phases, implying that the reaction pathway can be well defined along the changing lattice parameters. These lattice parameters can also represent detailed atomic reorganizations reasonably in most cases because they are the results of atomic species and their bond structures.

We then define the energy penalty associates with the lattice parameter mismatch as the lattice mismatch energy (LME). Note that this LME does not contain detailed atomic interactions owing to the adjacent phase that do not cause any lattice changes. Fig. 5*B* shows the calculated LME of VODP between the pristine and intermediate phases ($E_{PRI||INT}$), the intermediate and fully charged phases ($E_{INT||CHG}$), and the pristine and fully charged phases ($E_{PRI||CHG}$), where the latter is a hypothetical case. For the reaction coordinate, sets of lattice parameters, {a,b}, {a,c}, {b,c}, and {a,b,c}, were used under the assumption that they evolve linearly from one phase to another phase. For example, the {a,b} indicates that the lattice constants a and b are altered gradually along the constrained reaction path between two phases, whereas the c parameter is freely relaxed. That is, {a,b} indicates the LME perpendicular to the ab plane (or the LME along the c direction). In the same manner, {a,c} and {b,c} are the LME along the b and a directions, respectively. The most constrained, {a,b,c}, can be considered as the averaged upper bound of the LME. With these definitions, the following points are noteworthy in Fig. 5*B*.

First, along all of the directions, the LME between the pristine and intermediate phases ($E_{PRI||INT}$ = 11–12 meV) is lower than that between the intermediate and fully charged phases

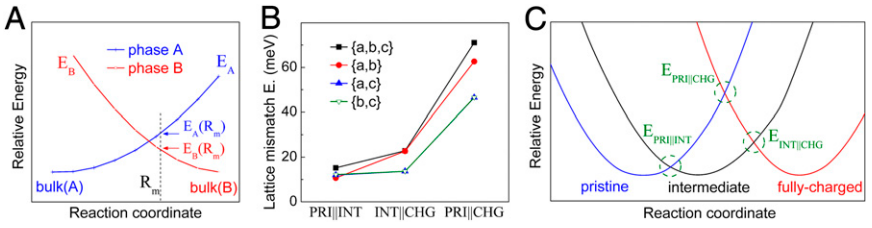

Fig. 5. (*A*) Relative energies of phases A and B as a function of geometry changes. The minimum value of the total energy penalties, $E_A(R_m) + E_B(R_m)$, is the activation energy. (*B*) The lattice mismatch energies between the pristine and intermediate phases (PRI||INT), the intermediate and fully charged phases (INT||CHG), and the pristine and fully charged phases (PRI||CHG). (*C*) The presence of intermediate phase reduces the lattice mismatch energy that should be overcome for the phase boundary migration.

($E_{INT||CHG}$ = 14–23 meV). We expect that this smaller LME for the first plateau is the origin of the smaller polarization observed in Fig. 2*C*.

Second, the $E_{PRI||INT}$ is almost identical in all of the directions; therefore, the (de)insertion process between pristine and intermediate phases is isotropic in terms of LME. However, the $E_{INT||CHG}$ along the c direction (red line in Fig. 5*B*) is higher than that along the other directions by ∼10 meV, implying the (de)insertion process could have directionality in the second half of the charge as in the $LiFePO_4$. Note that the anisotropy of LME in $LiFePO_4$ is 12–35 meV with the lowest value along the a direction, consistent with experiments (37).

Third, more importantly, the LME for the hypothetical two-phase reaction between pristine and fully charged phases in the absence of an intermediate phase ($E_{PRI||CHG}$) is notably higher than the $E_{PRI||INT}$ and $E_{INT||CHG}$, as well as the sum of them, suggesting that the presence of intermediate phases can enhance the cell kinetics by reducing LME. Fig. 5*C* shows this interpretation schematically in the relative energy vs. reaction coordinate picture. When the lattice parameters or volume is set as the reaction coordinate, the energy curves of each phase are generally quadratic as a function of reaction coordinate (38, 39). In such a case, the TSs of each biphasic reaction locate around the cross point (dashed circles in Fig. 5*C*) owing to the similar elastic moduli between two phases, implying that the smaller difference in reaction coordinate would yield the lower activation barrier for the reaction. In this manner, the presence of intermediate phases can improve the cell kinetics by buffering the differences in the lattice parameters.

As another example, the vanadium-based NASICON structure $Na_3V_2(PO_4)_3$ exhibits a single plateau without intermediate phases at low current rates; however, it shows a peak split at high current rates, as in the VODP (40). In the fast charge/discharge conditions, thermodynamically inaccessible intermediate phases in slow rates can be viable owing to the increased polarizations. In such cases, kinetics determines the reaction pathway whether through the intermediate phase or not. The split peak at high rate indicates that the reaction pathway through the intermediate phase is favorable in kinetics when both pathways are thermodynamically allowed. In other words, even for the unstable intermediate phases, if their energy level is shallow enough the presence of intermediate phases is beneficial for cell kinetics in fast rate conditions. Likewise, we expect that the small polarization and high rate capability of $Na_4Co_3(PO_4)_2P_2O_7$ are also attributed to the multiple intermediate phases with small lattice differences (41).

However, because the intermediate phases always involve corresponding voltage steps, the single-valued plateau observed in our material is rather unusual. Similarly, the single-phase reaction, which can be considered as an infinite sequence of two-phase reactions via countless "intermediate phases" that are infinitesimally different, provides better kinetics for the reasons described above but typically shows a sloping voltage behavior. In this point of view, VODP retains remarkably the advantages of both two-phase reaction (well-defined voltage) and a single-phase reaction (improved kinetics) owing to the intermediate phase with a small energy difference.

Conclusions

We have discovered an SIB cathode material, $Na_7V_4(P_2O_7)_4PO_4$, or VODP, that exhibits single well-defined plateaus at 3.88 V vs. Na/Na^+ throughout the entire capacity range. A theoretical analysis reveals that the very shallow energy level of an intermediate phase owing to the iso-energetic structural rearrangements (charge ordering and framework rotation) is the origin of this single-valued voltage behavior. We suggested a simple way to quantify activation barriers for two-phase (de)insertion reactions, yielding an intuitive conclusion that the smaller changes in lattice parameters lead to the lower reaction barriers. By extension, as a rule of thumb, we show that the presence of intermediate phases can reduce reaction barriers by buffering the differences in lattice parameters between two end members, giving a better kinetics.

Although the presence of such stable intermediate phases is an intrinsic property of materials that is not easy to tune, using intermediate phases is a useful concept to improve kinetic properties of battery materials. This approach may be achievable, for example, by controlling the size of particles, which can alter the reaction free energy curves (42). Also, the well-behaved high voltages and impressive cycling and rate capability of VODP would be a significant step forward to make functional SIB systems in the near future.

Materials and Methods

Synthesis. $Na_7V_4(P_2O_7)_4PO_4$ (VODP) was synthesized by conventional solid-state reaction. Stoichiometric amounts of Na_2CO_3 (≥99.5%; Aldrich), V_2O_5 (≥98%; Aldrich), and $NH_4H_2PO_4$ (≥99.9%; Aldrich) were mixed by ball-milling in the presence of acetone for 2 d, and acetone was then evaporated at 80 °C. Next, the mixture was dried in an oven at 70 °C overnight and was then pelletized. The pellets were heat-treated at 250 °C for 3 h under argon flow. The pellets were cooled down to room temperature and were ground once again in a mortar to ensure uniform mixing between the precursors. Finally, the mixture was reacted at 800 °C for 6 h under argon flow, completing the synthesis of VODP. rGO was obtained by first preparing graphene oxide (GO) suspension from commercial graphite (Alfa Aesar) based on a modified Hummer's method. In this method, 1 g of graphite was oxidized in an acid solution where 0.5 g of sodium nitrate ($NaNO_3$; Aldrich) and 3.5 g of potassium permanganate ($KMnO_4$; Aldrich) were dissolved in 23 mL of sulphuric acid (Aldrich). Then, the graphite oxide suspension was sonicated for exfoliation. Finally, the 200-mL GO suspension (1 $mg{\cdot}mL^{-1}$) was reduced by introducing 400 μL of hydrazine monohydrate ($N_2H_4{\bullet}H_2O$; Sigma Aldrich), and the solution was then refluxed at 98 °C for 5 h. The final suspension was filtered and washed with deionized water and ethanol several times to remove any impurities. For rGO $Na_7V_4(P_2O_7)_4PO_4$, VODP and rGO were mixed using low-energy ball milling for 12 h. Then, the mixture was heat-treated in a furnace at 200 °C for 1 h under argon atmosphere to facilitate electrically better contacts between both components.

Crystal Structure Characterization. Powder X-ray diffraction measurements were carried out with a Rigaku DMAX-2200PC X-ray diffractometer equipped with a graphite monochromator (λ = 1.5418 Å). A step scan mode was used in the 2θ range of 10.10–110° with a step size of 0.02° and counting time of 5 s for each step. Neutron powder diffraction data were obtained with a high resolution powder diffractometer at Hanaro Center of Korea Atomic Energy Research Institute. A vanadium canister was used as a sample holder. The data were collected in the 2θ range of 0–159.95° with a step size of 0.05°. The refinements of XRD and ND data were carried out by the Rietveld method with the Fullprof program (43). For ex situ XRD characterization of the battery cycled electrodes, a multipurpose attachment X-ray diffractometer (D/Max-2500; Rigaku) with Cu Kα was used in the 2θ range of 10–31° at a scan rate of $1°{\cdot}min^{-1}$.

Electrochemical Tests. The battery electrodes were fabricated by first making slurries. For the pure VODP, the active material, super P, and poly(vinylidene fluoride) (PVDF) were dispersed in *N*-methyl-2-pyrrolidone (99.5%; Aldrich) in a mass ratio of 6: 3: 1. In the case of rGO $Na_7V_4(P_2O_7)_4PO_4$, the slurry was made in a mass ratio of VODP: rGO: super P: PVDF of 6: 1.5: 1.5: 1. The slurries were cast onto the aluminum foils and were then dried inside a vacuum oven at 70 °C for 12 h. The mass loading of the active material was 2.0 $mg{\cdot}cm^{-2}$ for all of the samples. For the actual electrochemical tests, 2,032 coin-type half cells were assembled by using sodium thin disks as both the reference and counter electrodes. One molar sodium perchlorate (98.0%; Aldrich) ($NaClO_4$) in cosolvent of ethylene carbonate (99.9%, anhydrous; Aldrich) and propylene carbonate (99.7%, anhydrous; Aldrich) with a 1:1 volume ratio was used as electrolyte. The final cells were assembled by sandwiching polyethylene separators (Celgard 2400) between the active electrodes and the sodium thin disks in a glove box. The electrochemical properties were assessed by galvanostatic measurements in the voltage range of 2.0–4.2V (vs. Na/Na^+) with a battery cycler (WBCS 3000; Wonatech Co.). The QOCP measurements were done at C/20 with a 2-h relaxation time before potential acquisition at each data point. Detailed C-rate conditions

are presented in figure legends. All of the C rates addressed in this paper are with respect to 1 C (92.8 $mA{\cdot}g^{-1}$), not actual charge/discharge durations.

DFT Calculations. For the voltage and formation energy calculations, up to the 70 lowest electrostatic energy configurations at each composition were sampled and fully optimized with the Vienna Ab initio Simulation Package (44, 45). We adopted the projector-augmented wave method (46) and Perdew–Burke–Ernzerhof exchange-correlation functional (47) with Hubbard parameters (U_{eff} = 4.5 eV for vanadium) to address the self-interaction energy (48). We used a plane wave basis set with an energy cutoff of 520 eV and sampling the $2 \times 2 \times 4$ Monkhorst–Pack k-point mesh (49). The $1 \times 1 \times 2$ supercells were additionally explored to determine the intermediate phase at the $x = 5$ composition. Rotation barriers were calculated with the nudged elastic band method (50). All crystal structures were visualized with VESTA software (51).

ACKNOWLEDGMENTS. This work was financially supported by National Research Foundation of Korea Grants NRF-2010-0029031 and NRF-2009-0094046 funded by the Korean Ministry of Science and Technology and Qatar National Research Fund NPRP 5-569-2-232. S.Y.L. acknowledges the National Research Foundation of Korea for the NRF-2013-Global PhD Fellowship Program. The generous computing time from the Korea Institute of Science and Technology Information is also gratefully acknowledged.

1. Ellis BL, Nazar LF (2012) Sodium and sodium-ion energy storage batteries. *Curr Opin Solid St* 16(4):168–177.
2. Palomares V, et al. (2012) Na-ion batteries, recent advances and present challenges to become low cost energy storage systems. *Energy Environ Sci* 5(3):5884–5901.
3. Berthelot R, Carlier D, Delmas C (2011) Electrochemical investigation of the P2–NaxCoO2 phase diagram. *Nat Mater* 10(1):74–80.
4. Buchholz D, et al. (2013) Toward Na-ion batteries-synthesis and characterization of a novel high capacity Na ion intercalation material. *Chem Mater* 25(2):142–148.
5. Caballero A, et al. (2002) Synthesis and characterization of high-temperature hexagonal P2-Na0.6MnO2 and its electrochemical behaviour as cathode in sodium cells. *J Mater Chem* 12(4):1142–1147.
6. Guignard M, et al. (2013) P2-Na(x)VO2 system as electrodes for batteries and electron-correlated materials. *Nat Mater* 12(1):74–80.
7. Komaba S, et al. (2012) Study on the reversible electrode reaction of Na(1-x)Ni(0.5)Mn(0.5)O2 for a rechargeable sodium-ion battery. *Inorg Chem* 51(11):6211–6220.
8. Sharma PK, Moore GJ, Zhang F, Zavalij P, Whittingham MS (1999) Electrical properties of the layered manganese dioxides MxMn1-yCoyO2, M = Na, K. *Electrochem Solid St* 2(10):494–496.
9. Yabuuchi N, et al. (2012) P2-type Na(x)[Fe(1/2)Mn(1/2)]O2 made from earth-abundant elements for rechargeable Na batteries. *Nat Mater* 11(6):512–517.
10. Yuan DD, et al. (2013) Synthesis and electrochemical behaviors of layered Na0.67Mn0.65Co0.2Ni0.15O2 microflakes as a stable cathode material for sodium-ion batteries. *J Mater Chem A* 1(12):3895–3899.
11. Shakoor RA, et al. (2012) A combined first principles and experimental study on Na3V2(PO4)2F3 for rechargeable Na batteries. *J Mater Chem* 22(48):20535–20541.
12. Sauvage F, Quarez E, Tarascon JM, Baudrin E (2006) Crystal structure and electrochemical properties vs. Na+ of the sodium fluorophosphate Na1.5VOPO4F0.5. *Solid State Sci* 8(10):1215–1221.
13. Barker J, Saidi MY, Swoyer JL (2003) A sodium-ion cell based on the fluorophosphate compound NaVPO4F. *Electrochem Solid St* 6(1):A1–A4.
14. Liu ZM, et al. (2008) Preparation of NaV(1-x)Al(x)PO4F cathode materials for application of sodium-ion battery. *T Nonferr Metal Soc* 18(2):346–350.
15. Zhuo HT, et al. (2006) The preparation of NaV1-xCrxPO4F cathode materials for sodium-ion battery. *J Power Sources* 160(1):698–703.
16. Barpanda P, et al. (2012) Sodium iron pyrophosphate: A novel 3.0 V iron-based cathode for sodium-ion batteries. *Electrochem Commun* 24:116–119.
17. Kim H, et al. (2013) Na2FeP2O7 as a promising iron-based pyrophosphate cathode for sodium rechargeable batteries: A combined experimental and theoretical study. *Adv Funct Mater* 23(9):1147–1155.
18. Park CS, et al. (2013) Anomalous manganese activation of a pyrophosphate cathode in sodium ion batteries: A combined experimental and theoretical study. *J Am Chem Soc* 135(7):2787–2792.
19. Casas-Cabanas M, et al. (2012) Crystal chemistry of Na insertion/deinsertion in FePO4-NaFePO4. *J Mater Chem* 22(34):17421–17423.
20. Moreau P, Guyomard D, Gaubicher J, Boucher F (2010) Structure and stability of sodium intercalated phases in olivine FePO4. *Chem Mater* 22(14):4126–4128.
21. Lee KT, Ramesh TN, Nan F, Botton G, Nazar LF (2011) Topochemical synthesis of sodium metal phosphate olivines for sodium-ion batteries. *Chem Mater* 23(16):3593–3600.
22. Oh SM, Myung ST, Hassoun J, Scrosati B, Sun YK (2012) Reversible NaFePO4 electrode for sodium secondary batteries. *Electrochem Commun* 22:149–152.
23. Lee H, Kim Y-I, Park J-K, Choi JW (2012) Sodium zinc hexacyanoferrate with a well-defined open framework as a positive electrode for sodium ion batteries. *Chem Commun (Camb)* 48(67):8416–8418.
24. Lu Y, Wang L, Cheng J, Goodenough JB (2012) Prussian blue: A new framework of electrode materials for sodium batteries. *Chem Commun (Camb)* 48(52):6544–6546.
25. Wessells CD, Huggins RA, Cui Y (2011) Copper hexacyanoferrate battery electrodes with long cycle life and high power. *Nat Commun* 2:550.
26. Lim SY, Kim H, Shakoor RA, Jung Y, Choi JW (2012) Electrochemical and thermal properties of NASICON structured Na3V2(PO4)(3) as a sodium rechargeable battery cathode: A combined experimental and theoretical study. *J Electrochem Soc* 159(9):A1393–A1397.
27. Zatovsky IV (2010) NASICON-type Na3V2(PO4)3. *Acta Crystallogr Sect E Struct Rep Online* 66(Pt 2):i12.
28. Delarochere M, Kahn A, Dyvoire F, Bretey E (1985) Crystal-structure and cation-transport properties of Na7(AlP2O7)4PO4, Na7(CrP2O7)4PO4, Na7(FeP2O7)4PO4. *Mater Res Bull* 20(1):27–34.
29. Padhi AK, Nanjundaswamy KS, Goodenough JB (1997) Phospho-olivines as positive-electrode materials for rechargeable lithium batteries. *J Electrochem Soc* 144:1188–1194.
30. Ong SP, et al. (2011) Voltage, stability and diffusion barrier differences between sodium-ion and lithium-ion intercalation materials. *Energy Environ Sci* 4(9):3680–3688.
31. Bak SM, et al. (2011) Spinel LiMn2O4/reduced graphene oxide hybrid for high rate lithium ion batteries. *J Mater Chem* 21(43):17309–17315.
32. Kim HK, Bak SM, Kim KB (2010) Li4Ti5O12/reduced graphite oxide nano-hybrid material for high rate lithium-ion batteries. *Electrochem Commun* 12(12):1768–1771.
33. Rui XH, et al. (2011) Reduced graphene oxide supported highly porous V2O5 spheres as a high-power cathode material for lithium ion batteries. *Nanoscale* 3(11):4752–4758.
34. Zhou XF, Wang F, Zhu YM, Liu ZP (2011) Graphene modified LiFePO4 cathode materials for high power lithium ion batteries. *J Mater Chem* 21(10):3353–3358.
35. Meethong N, Huang H-YS, Speakman SA, Carter WC, Chiang Y-M (2007) Strain accommodation during phase transformations in olivine-based cathodes as a materials selection criterion for high-power rechargeable batteries. *Adv Energy Mater* 17:1115–1123.
36. Van der Ven A, Wagemaker M (2009) Effect of surface energies and nano-particle size distribution on open circuit voltage of Li-electrodes. *Electrochem Commun* 11:881–884.
37. Chen G, Song X, Richardson TJ (2006) Electron microscopy study of the LiFePO4 to FePO4 phase transition. *Electrochem Solid St* 9:A295.
38. Birch F (1947) Finite elastic strain of cubic crystals. *Phys Rev* 71:809–824.
39. Murnaghan FD (1944) The compressibility of media under extreme pressures. *Proc Natl Acad Sci USA* 30(9):244–247.
40. Saravanan K, Mason CW, Rudola A, Wong KH, Balaya P (2012) The first report on excellent cycling stability and superior rate capability of Na3V2(PO4)3 for sodium ion batteries. *Adv Energy Mater* 3(4):444–450.
41. Nose M, et al. (2013) Na4Co3(PO4)2P2O7: A novel storage material for sodium-ion batteries. *J Power Sources* 234(0):175–179.
42. Van der Ven A, Garikipati K, Kim S, Wagemaker M (2009) The role of coherency strains on phase stability in LixFePO4: Needle crystallites minimize coherency strain and overpotential. *J Electrochem Soc* 156:A949–A957.
43. Rodriguez-Carvajal J (1993) Recent advances in magnetic structure determination by neutron powder diffraction. *Physica B* 192:55–69.
44. Aydinol MK, Kohan AF, Ceder G, Cho K, Joannopoulos J (1997) Ab initio study of lithium intercalation in metal oxides and metal dichalcogenides. *Phys Rev B* 56(3):1354–1365.
45. Kresse G, Furthmuller J (1996) Efficiency of ab-initio total energy calculations for metals and semiconductors using a plane-wave basis set. *Comput Mater Sci* 6(1):15–50.
46. Blöchl PE (1994) Projector augmented-wave method. *Phys Rev B Condens Matter* 50(24):17953–17979.
47. Perdew JP, Burke K, Ernzerhof M (1996) Generalized gradient approximation made simple. *Phys Rev Lett* 77(18):3865–3868.
48. Dudarev SL, Botton GA, Savrasov SY, Humphreys CJ, Sutton AP (1998) Electron-energy-loss spectra and the structural stability of nickel oxide: An LSDA+U study. *Phys Rev B* 57(3):1505–1509.
49. Monkhorst HJ, Pack JD (1976) Special points for brillouin-zone integrations. *Phys Rev B* 13(12):5188–5192.
50. Mills G, Jonsson H, Schenter GK (1995) Reversible work transition-state theory - application to dissociative adsorption of hydrogen. *Surf Sci* 324(2–3):305–337.
51. Momma K, Izumi F (2008) VESTA: a three-dimensional visualization system for electronic and structural analysis. *J Appl Cryst* 41:653–658.